Subtropical Contribution to Sub-Antarctic Mode Waters

Bieito Fernández Castro[1] [ID], **Matthew Mazloff[2]** [ID], **Richard G. Williams[3]** [ID], and **Alberto C. Naveira Garabato[1]** [ID]

[1]Ocean and Earth Science, National Oceanography Centre, University of Southampton, Southampton, UK, [2]Scripps Institution of Oceanography, La Jolla, CA, USA, [3]Department of Earth Ocean and Ecological Sciences, School of Environmental Sciences, University of Liverpool, Liverpool, UK

Abstract Sub-Antarctic Mode Waters (SAMW) form to the north of the Antarctic Circumpolar Current (ACC) through deep winter mixing. SAMW connect the atmosphere with the oceanic pycnocline, transferring heat and carbon into the ocean interior and supplying nutrients to the northern ocean basins. The processes controlling SAMW ventilation and properties remain poorly understood. Here, we investigate the significance and origin of a ubiquitous feature of SAMW formation regions: The seasonal build-up of a subsurface salinity maximum. With biogeochemical Argo floats, we show that this feature influences SAMW mixed-layer dynamics, and that its formation is associated with a decline in preformed nutrients comparable to biological drawdown in surface waters ($\sim$0.15 mol m^{-2} y^{-1}). Our analysis reveals that these features are driven by advection of warm, salty, nutrient-poor waters of subtropical origin along the ACC. This influx represents a leading-order term in the SAMW physical and biogeochemical budgets, and can impact large-scale nutrient distributions.

Plain Language Summary Sub-Antarctic Mode Waters (SAMW) form during vigorous, deep winter mixing at the northern edge of the Antarctic Circumpolar Current (ACC). SAMW constitute an important portion of the upper ocean volume, and slow down climate change by storing vast amounts of anthropogenic heat and carbon. SAMW also transport Southern Ocean nutrients toward lower latitudes, sustaining primary productivity around and north of the tropics. Using data from biogeochemical Argo floats, we investigate the seasonal dynamics of SAMW formation, which are hitherto poorly understood due to the region's remoteness and harsh winter conditions. We show that SAMW formation regions feature the seasonal build-up of a subsurface salinity maximum along with a decrease in nutrient levels, which are the imprint of the along-ACC transport of salty, nutrient-poor waters of subtropical origin. These findings highlight the important contribution of subtropical waters to SAMW heat, salt and nutrient budgets, which contrasts with the widespread view that SAMW form primarily through atmospheric lightening of cold, fresh Antarctic waters. These diverse views involve different feedback mechanisms between climate and SAMW formation and have divergent implications for understanding the impacts of climate change on heat and carbon sequestration, and nutrient redistribution, by SAMW.

1. Introduction

Sub-Antarctic Mode Waters (SAMW) are a central component of the ocean's large-scale circulation, constituting together with Antarctic Intermediate Waters (AAIW) the northward-flowing branch of the upper meridional overturning cell in the Southern Ocean. The subduction of SAMW and AAIW compensates for the upwelling of deeper, southward-flowing Circumpolar Deep Waters along the sloping density surfaces of the Antarctic Circumpolar Current (ACC) (Marshall & Speer, 2012; Sloyan & Rintoul, 2001). SAMW ventilate the lower pycnocline of the subtropical gyres (Jones et al., 2016; McCartney, 1982; Morrison et al., 2022), playing a major role in a series of important climate-related processes. SAMW are responsible for a substantial fraction of global uptake and storage of anthropogenic heat (Roemmich et al., 2015) and carbon (Gruber et al., 2019; Sabine et al., 2004) and, in returning nutrients from the Southern Ocean to the northern ocean basins, sustain biological production and carbon export there (Sarmiento et al., 2004).

SAMW form through convective mixing in a relatively narrow latitudinal band of deep (>300 m) winter mixed-layers in the sub-Antarctic zone (SAZ), north of the sub-Antarctic front (SAF) at the ACC's equatorward edge (Hanawa & Talley, 2001; Holte & Talley, 2009). Deep mixed-layers leading to SAMW production occur mostly in the central and eastern Pacific and Indian oceans (Sallée et al., 2010). These formation regions are

associated with SAMW pools of different properties, becoming progressively fresher, cooler, and denser from the western Indian to the eastern Pacific Ocean (Herraiz-Borreguero & Rintoul, 2011; Li et al., 2021; Sallée et al., 2010). The ventilation of the SAMW pools takes place through the subduction of fluid from the deep mixed-layers at the end of winter (Williams et al., 1995). Therefore, the properties of SAMW are a consequence of the processes which, acting over the previous annual cycle, determine winter mixed-layer characteristics. Such processes include air-sea fluxes (Holte et al., 2012; McCartney, 1977), northward Ekman transport of cool, fresh upper-ocean waters across the ACC (Rintoul & England, 2002), eddy-induced cross-frontal exchanges (Herraiz-Borreguero & Rintoul, 2010; Holte et al., 2013; Sallée et al., 2008) and advection of subtropical waters by the gyre- and mesoscale circulation (Small et al., 2021; Wang et al., 2014). Quantifying the variable interplay between these contributions is key to understand the sensitivity of SAMW formation rates and properties to climate variability (Gao et al., 2018; Meijers et al., 2019; Naveira Garabato et al., 2009; Portela et al., 2020; Qu et al., 2020; Rintoul & England, 2002), as well as the implications for oceanic heat (Gao et al., 2018) and carbon (Hauck et al., 2013) storage and the fertilization of low-latitude oceans (Ayers & Strutton, 2013).

Despite recent efforts, the balance of processes controlling the physical and biogeochemical properties of SAMW is only partially understood. Although modeling studies have documented the relevance of the contribution of subtropical waters to SAMW volume and property budgets, with a specific focus on anthropogenic carbon (Groeskamp et al., 2016; Iudicone et al., 2011, 2016), this contribution has received comparably little attention and remains poorly constrained with observations. Here, we shed light on this problem by using observations with biogeochemical (SOCCOM) and regular Argo floats to unravel the seasonal dynamics of SAMW formation regions. In particular, we investigate the origin and significance of a conspicuous feature characterizing these regions: The seasonal formation of a subsurface salinity maximum (DuVivier et al., 2018; Holte et al., 2012). We show that this feature arises from the advection along the northern flank of the ACC of warm, saline, nutrient-poor waters of subtropical origin, and assess the relevance of this transport for the SAMW heat, salt and nutrient budgets. The study focuses on the SAMW formation regions of the Indian Ocean, but our main conclusions hold for the Pacific (detailed results in that region presented in the Supporting Information).

2. Methods

2.1. Seasonal Means in the SAMW Formation Regions

The seasonal dynamics at the SAMW formation sites were investigated by computing seasonal means of conservative temperature (θ), absolute salinity (S_A) (McDougall & Barker, 2011), neutral density (γ_n) (Jackett & McDougall, 1997), large-scale potential vorticity (PV) and nitrate (NO_3) using profiles (0–2,000 m) collected by SOCCOM biogeochemical Argo floats (Johnson, Plant, Coletti, et al., 2017; Talley et al., 2019) within three longitude-latitude boxes encompassing the SAMW formation areas in the eastern Indian (90°E–160°E, 40°S–52°S), and central (200°E–240°E, 45°S–55°S) and eastern Pacific (300°E–360°E, 50°S–60°S). The SOCCOM data set includes data from 267 floats between January 2009 and May 2021. Prior to time-averaging, the profiles were mapped onto a homogeneous vertical grid of 5 m. Then, seasonal cycles were calculated at 1-day intervals using a running Gaussian-weighted mean with an e-folding time of 60 days. The mixed-layer depth (MLD, or h) calculation followed a density difference criterion with respect to 10 m depth (de Boyer Montégut, 2004). The density threshold was 0.03 kg m⁻³ for in situ profiles and 0.125 kg m⁻³ for seasonal-mean profiles. Large-scale potential vorticity was estimated as $PV = (f/\rho)(\partial\rho/\partial z)$, where g is gravity and ρ is a potential density, $\rho = 1,000 + \gamma_n$.

2.2. Lagrangian Particle-Tracking

Particle-tracking experiments were performed to assess the origin of the water masses reaching the SAMW formation regions, and to test whether the formation of the subsurface salinity maximum may be explained by salt advection by the large-scale flow, for which we focus on horizontal geostrophic transport pathways below the surface Ekman layer. One thousand virtual particles were released at the depth of the salinity maximum at random locations within areas of deep mixed-layers (maximum annual MLD >500 m) and advected horizontally backwards in time using annual-mean geostrophic velocities. Those were computed from the annual-mean density field derived from the Roemmich and Gilson (2009) Argo climatology and referenced to a no-motion level at 2,000 m depth. The particles were tracked for 1 year and the time-integration was completed with a fourth

order Runge-Kutta scheme in 1-day time-steps. Unresolved eddy diffusion was accounted for by introducing a random-walk term (e.g., Ross & Sharples, 2004) with a horizontal diffusivity of 1,000 m^2 s^{-1}, a representative value for the Southern Ocean (Gille et al., 2022), but this choice had little impact on the results. Salinity at the particles' positions was obtained through linear interpolation of the annual-mean fields from Roemmich and Gilson (2009). In this way, we implicitly accounted for the mean diabatic transformations affecting the water mass properties along particle trajectories, which are not explicitly resolved in our analysis.

2.3. Upper-Ocean Heat and Salinity Budgets

The contribution of transport processes to SAMW properties was assessed with annual-mean upper-ocean budgets using monthly climatological data (Roemmich & Gilson, 2009). Specifically, the monthly salinity budget was computed by vertically integrating the following equation from the surface to the annual maximum MLD at each grid-point of the climatology:

$$\frac{\partial S_A}{\partial t} = -\left(u_{\text{geos}} + u_{\text{Ekm}} + u_{\text{eddy}}\right)\frac{\partial S_A}{\partial x} - \left(v_{\text{geos}} + v_{\text{Ekm}} + v_{\text{eddy}}\right)\frac{\partial S_A}{\partial y} + \mathcal{R}, \tag{1}$$

where $\partial S_A/\partial t$ is the monthly temporal trend; $\partial S_A/\partial x$ and $\partial S_A/\partial y$, the zonal and meridional gradients, respectively; u_{geos} (resp. v_{geos}), u_{Ekm} (resp. v_{Ekm}) and u_{eddy} (resp. v_{eddy}) are the eastward (resp. northward) geostrophic, Ekman and eddy-induced velocities; and $\mathcal{R}$ is a residual term calculated as the difference between the right-hand and left-hand terms. $\mathcal{R}$ is assumed to be dominated by air-sea fluxes, but also includes contributions from other neglected processes, such as diapycnal mixing and upwelling across the maximum MLD. Geostrophic velocities were calculated from monthly density fields, referenced to 2,000 m. Horizontal Ekman velocities were derived from monthly wind stress from the data-assimilative Biogeochemical Southern Ocean State Estimate (B-SOSE) (Verdy & Mazloff, 2017). The eddy-induced velocities were calculated with the Gent and McWilliams (1990) parameterization and an eddy diffusivity computed following Visbeck et al. (1997) (Supporting Information S1). The procedure is repeated with a heat budget using $\rho c_p \theta$ instead of S_A, where c_p is the specific heat capacity.

3. Seasonal Dynamics at the SAMW Formation Sites

Hydrographic properties display comparable seasonal patterns in the SAMW formation areas in the eastern Indian (Figure 1), and central (Figure S1 in Supporting Information S1) and eastern Pacific (Figure S2 in Supporting Information S1). In the Indian sector, mixed-layer temperature (θ) is maximum (10.5°C) in February–April, when the mixed-layer is shallowest (<100 m), and minimum (8.5°C) in August-October, when the mixed-layer is deepest (~400 m) (Figure 1b). mixed-layer salinity (S_A) is minimal in June (34.66 g kg^{-1}) and maximal (34.74 g kg^{-1}) in November (Figures 1c and 1e). Between 200 and 600 m depth, low PV (<0.5 × 10^{-10} m^{-1} s^{-1}) denotes the presence of the weakly stratified SAMW pool, in the γ_n = 26.9–27.1 kg m^{-3} range (Figure 1d). In the seasonal pycnocline –between the summer and winter mixed-layer bases–, θ and S_A display marked seasonal cycles, with amplitudes of ~0.4°C (8.6–9.0°C) and ~0.7 g kg^{-1} (34.73–34.8 g kg^{-1}), respectively, and maximum values in fall (April–June, Figures 1b–1d). The amplitude of the subsurface salinity cycle is comparable to that in the mixed-layer, even if not directly influenced by air-sea fluxes or Ekman transport. The θ-S_A variations are almost density-compensated (Figure 1d), but not fully, contributing to the re-stratification of the SAMW pool with a moderate PV increase from spring to late fall (Figure 1e).

As a consequence of these patterns, a salinity maximum develops over summer at 150–200 m depth, capping the SAMW pool, and is subsequently eroded by deep winter mixing. This subsurface salinity maximum enhances stratification at the mixed-layer base, conditioning its seasonal evolution (Figure 1f). This figure shows the rate of mixed-layer deepening (dh/dt) and the contributions to stratification at the mixed-layer base by salinity (N_S^2) and temperature (N_θ^2). The mixed-layer deepens from January, with the deepening rate accelerating gradually to ~1 m d^{-1} by April. Before March, stratification is temperature-dominated (2 × 10^{-5} s^{-2}), with a smaller salinity contribution (<1 × 10^{-5} s^{-2}). From March, the mixed-layer feels the influence of the salinity maximum, and salinity stratification gains relevance. Mixed-layer deepening accelerates to ~2 m d^{-1} in May-June, when haline stratification becomes dominant, as the mixed-layer reaches the salinity maximum's upper edge. When the mixed-layer crosses the salinity maximum, deepening accelerates sharply at ~7 m d^{-1}, favored by neutral/inverse haline
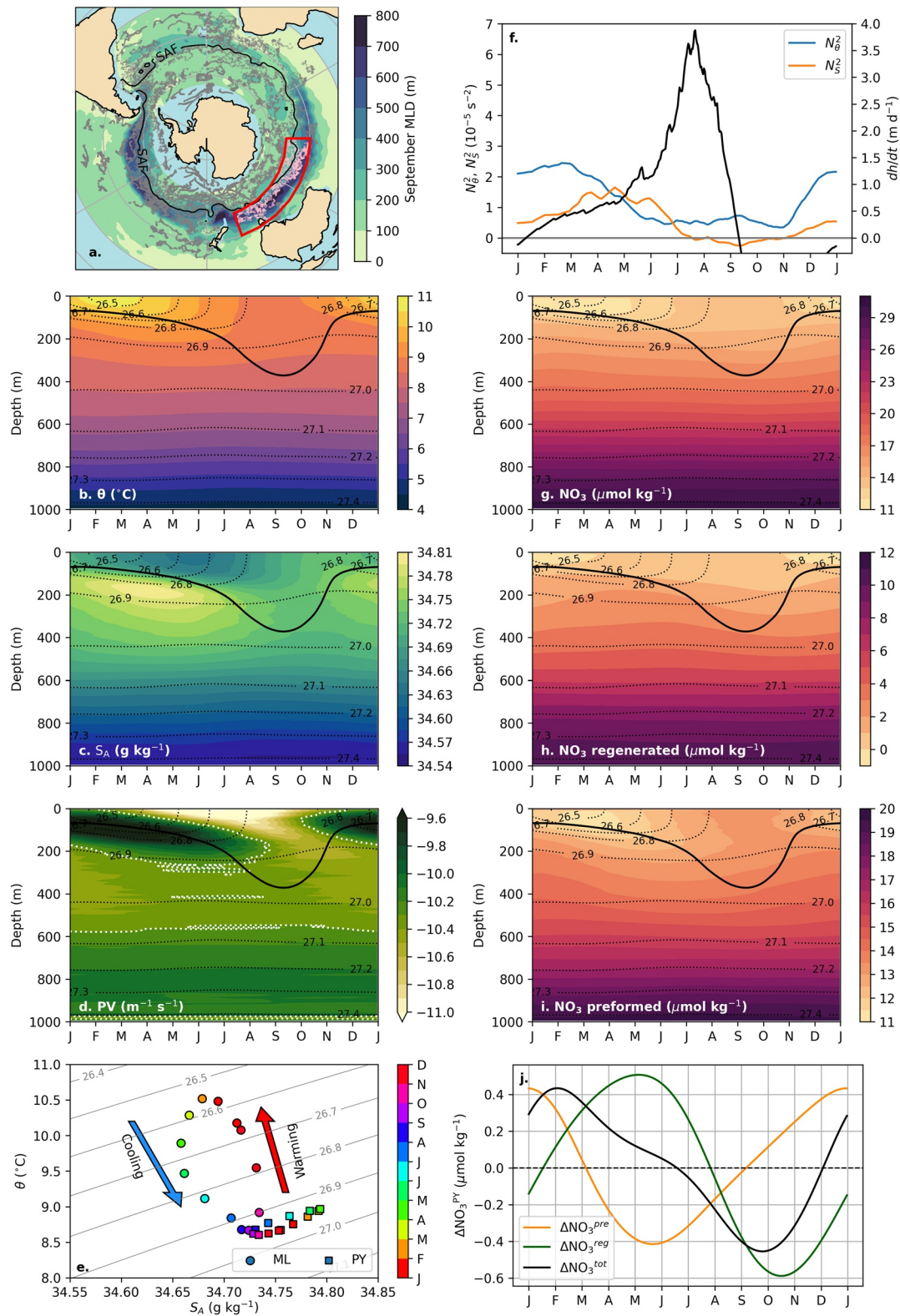
Figure 1.

stratification. The mixed-layer then reaches its maximum annual extent. These non-linear mixed-layer dynamics are illustrated with observations by float WMO5903593 at 100–110°E, 42–47°S between August 2013 and October 2014 (Figures 2a and 2b). This float was chosen because of its small displacement over the course of 1 year, sampling a relatively small geographic area. The float data shows the formation of the salinity maximum below the mixed-layer during summer, and the slow mixed-layer progression from January to August, followed by a sharp deepening down to 600 m, after the salinity maximum was crossed.

4. Origin of the Subsurface Salinity Maximum

The Lagrangian experiments show that a significant fraction of the particles reaching the seasonal pycnocline at SAMW formation sites with the mean geostrophic flow are advected from the west (Figure 3a). The mean salinity change along particle trajectories is consistent with the seasonal salinity evolution described above, in that salinity increases by ∼0.7 g kg^{-1} after 1 year of simulation (Figure 3b). The increase is larger (>1 g kg^{-1}) for the particles initialized at the southern rim of the SAMW formation region, which originate further west. These findings suggest that the formation of the salinity maximum is driven by advection along the ACC's northern flank of saltier waters originating at the western portion of the basin, where subtropical pycnocline waters flowing southeastward in the western boundary currents (at the Agulhas Current and Retroflection in the Indian Ocean) interleave with the northern ACC waters, increasing their salinity (Pollard & Read, 2001; Wang et al., 2014). Comparable salinity increases were found along geostrophic pathways in the Pacific (Figures S3 and S4 in Supporting Information S1).

To corroborate that the salinity maximum is generated by geostrophic advection, we used climatological Argo data to compute geostrophic salt transport in the region sampled by float WMO5903593 (Figure 2). The seasonal salinity evolution inferred from the Argo climatology (Figure 2d) in the float-sampled area (cyan box in Figure 2a) follows the same pattern as the direct observations, as well as the seasonal cycle described above (Figures 1c and 2b). Salt convergence by geostrophic transport is maximum (0.3 g kg^{-1} yr^{-1}) at the top of the seasonal pycnocline (150–400 m) during summer, in coincidence with the salinity maximum, and exhibits weak values below the SAMW pool (below 27.0 kg m^{-3}) (Figure 2e). The time-integrals of the salt convergence (dashed lines in Figure 2f) closely track the salinity increase between January and July at different depths within the seasonal pycnocline, confirming that the salinity maximum build-up can be explained by geostrophic advection.

5. Contribution to SAMW Heat and Salinity Budgets

We next assess the influence of geostrophic transport in the heat and salinity budgets of the SAMW formation sites. Budget terms averaged in a 5-degree latitudinal band to the north of the SAF indicate that Ekman transport cools and freshens the SAZ. Ekman cooling and freshening are maximal around the Kerguelen Plateau (75°E), and minimal in the western Pacific, downstream of the Campbell Plateau (170–190°E), and in the eastern Pacific, upstream of Drake Passage (260°E–300°E) (Figures 4c and 4e). Northward Ekman fluxes are compensated by warming and salinification by southeastward geostrophic and eddy transfers. The sign of the residuals representing the air-sea flux varies zonally, but corresponds mainly to cooling and freshening, more consistently in the Pacific. Geostrophic warming and salinification are maximal in the Indian Ocean within 50°E–140°E, downstream of the Agulhas region where eddy warming and salinification reach their circumpolar maxima (Figures 4c, 4,e and S5).

The budget terms averaged in the areas of deep mixed-layers (>500 m) show that, at the eastern Indian SAMW formation region (Figure 4d), Ekman freshening (−29 g kg^{-1} m yr^{-1}) is compensated by geostrophic salinification (+17 g kg^{-1} m yr^{-1}), with secondary contributions by air-sea (+8 g kg^{-1} m yr^{-1}) and eddy fluxes (+4 g kg^{-1} m yr^{-1}). In the central and eastern Pacific formation regions, freshening is effected through a combination

Figure 1. (a) Location of Southern Ocean Carbon and Climate Observations and Modeling (SOCCOM) float profiles (gray) in the Sub-Antarctic Mode Waters (SAMW) formation area of the eastern Indian Ocean (pink dots delimited by red box); (b) conservative temperature (θ); (c) absolute salinity (S_A); (d) potential vorticity (PV); (e) temperature-salinity diagram in the mixed-layer (ML) and in the pycnocline (PY); (f) rate of mixed-layer deepening (dh/dt, black) and thermal (N_θ^2, blue) and haline (N_S^2, orange) stratifications at the mixed-layer base; (g) total, (h) regenerated and (i) preformed nitrate (NO$_3$) and (j) their depth-averaged anomalies (Δ) with respect to the annual-mean in the seasonal pycnocline (PY). In (a), filled contours represent the mean September mixed-layer depth (MLD) from Roemmich and Gilson (2009) and the black contour, the sub-Antarctic Front (SAF) following the Naveira Garabato et al. (2009) definition. In b–d, g–i, the black thick line represents the mixed-layer depth (MLD); the gray dotted lines, neutral density, and the white dotted lines in (d), PV = 0.5 × 10^{-10} m^{-1} s^{-1}.
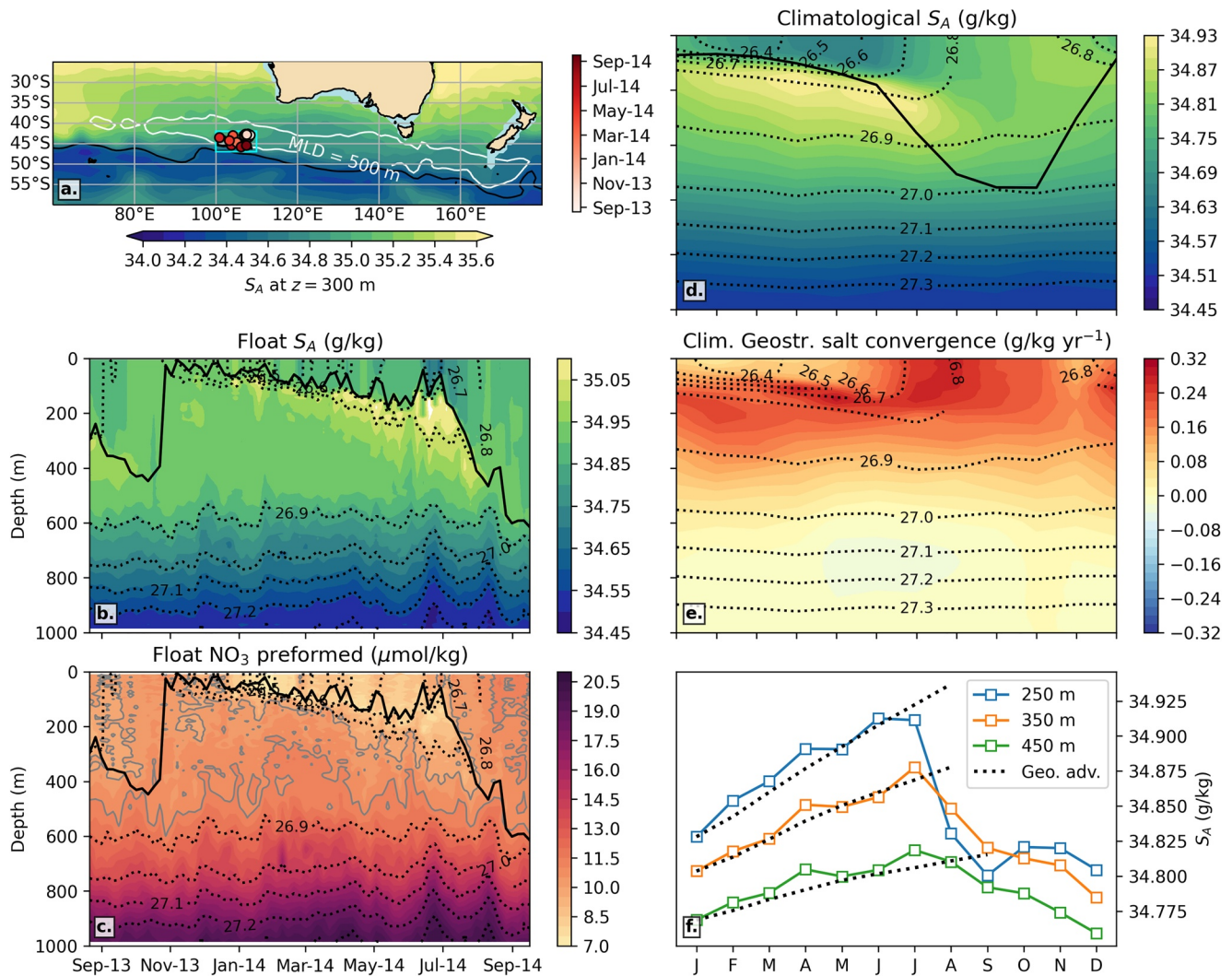
Figure 2. (a) Location of the profiles collected by float WMO5903593 between August 2013 and October 2014 in the eastern Indian Ocean (circles); (b) absolute salinity (S_A) and (c) preformed nitrate (NO_3) profiles recorded by the float, with the mixed-layer represented as a black thick line and isoneutrals as dotted lines; (d) mean seasonal S_A cycle from the Roemmich and Gilson (2009) climatology computed in the cyan box in (a); (e) salinity convergence due to geostrophic transport; (f) seasonal S_A trends at different depths within the cyan box and time-integrated geostrophic salt convergence (black dots). In (a), filled contours represent the annual-mean S_A at 300 m; white contours, the annual maximum mixed-layer depth (MLD) of 500 m, and the black contour, the SAF. Note that the y-axes in panels d and e are the same as in b and c.

of air-sea (−13 and −11 g kg^{-1} m yr^{-1}, respectively) and northward Ekman fluxes (−10 and −4 g kg^{-1} m yr^{-1}), balanced mainly by southeastward geostrophic advection (+20 and + 14 g kg^{-1} m yr^{-1}) and eddy transport (+3 and + 1 g kg^{-1} m yr^{-1}). Geostrophic heat advection is also the main warming term in all regions, opposing Ekman advection in all areas and atmospheric cooling over the eastern Pacific (Figure 4f), consistent with the heat budget in a regional ocean model (Tamsitt et al., 2016).

6. Influence on Nutrient Concentrations

To assess the biogeochemical relevance of the subtropical influx to SAMW, we examine nitrate seasonality in the Indian sector (Figures 1g and 1j). In the surface layer, nitrate follows the characteristic pattern of spring-summer depletion due to biological uptake (Johnson, Plant, Dunne, et al., 2017) and subsequent accumulation of organic matter (Figure S6 in Supporting Information S1). However, in the seasonal pycnocline, nitrate decreases over summer-fall, contrary to the expectation of organic matter remineralization prevailing in twilight layers (Arteaga
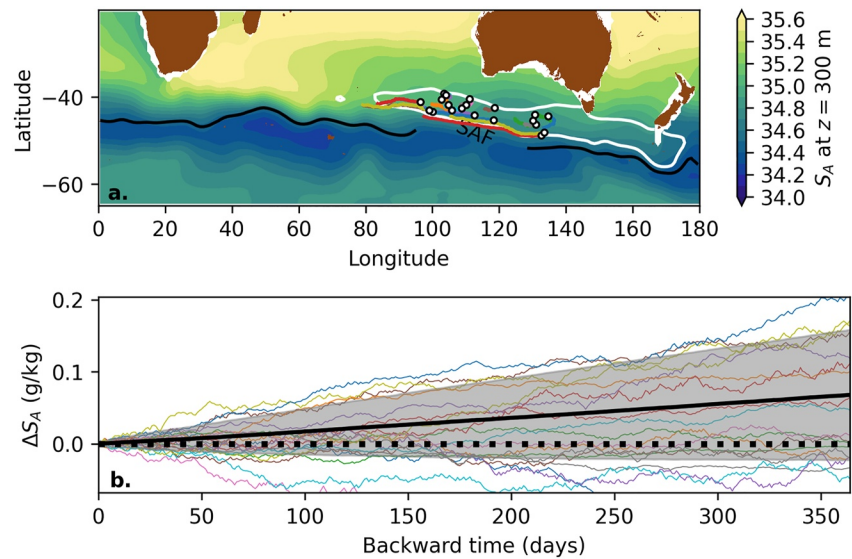
Figure 3. (a) Examples of the backwards trajectories of 20 Lagrangian particles following the geostrophic flow in the Indian Ocean (90°E–135°E), and (b), mean (black line) and standard deviation (shading) of the annual-mean absolute salinity change ($\Delta S_A = S_A(t) - S_A(t = 0)$) along backward trajectories. In (a), filled contours represent the climatological mean S_A at 300 m; black contour, the sub-Antarctic front (SAF); white contour, the seasonal maximum MLD of 500 m, and, white dots, the particles' initial positions.

et al., 2019). To explain this pattern, we decompose the nitrate signal into the regenerated ($NO_3^{reg} = R_{NO}AOU$, where AOU is the apparent oxygen utilization and $R_{NO} = 16/170$ the nitrogen:oxygen ratio of remineralization), and the preformed pools $\left(NO_3^{pre} = NO_3 - NO_3^{reg}\right)$ (Williams & Follows, 2011). The former pool accounts for nitrate released by remineralization, while the latter is a quasi-conservative tracer indicative of water masses of contrasting origin, with subtropical waters having lower preformed nitrate than subpolar waters. Note that NO_3^{reg} includes the effects of air-sea oxygen disequilibrium on AOU, but its contribution is secondary ($\sim$10%, Figure S7 in Supporting Information S1) in this region, and was neglected for the qualitative description of the system. The regenerated pool increases as expected in the summer pycnocline (Figures 1h and 1j), due to an enhancement in AOU (Figure S7), but the increase is overridden by a larger decrease in preformed nitrate ($\sim$0.8 μmol kg^{-1}, Figures 1i and 1j), concurrent to the salinity increase (as illustrated by the example float, Figures 2b and 2c). Similar patterns were observed in the Pacific (Figures S1 and S2 in Supporting Information S1).

These results suggest that the advection of subtropical waters with low preformed nitrate reduces nutrient concentrations in the SAMW formation region, as supported by the negative correlation between depth-averaged nitrate and salinity in the SAMW density range for all the float profiles in the Indian SAZ ($NO_3 \propto -11.1 S_A$, $r^2 = 0.816$, Figure S8e in Supporting Information S1) (see Figures S9 and S10 in Supporting Information S1 for similar results in the Pacific). This correlation is driven by the inverse relationship between preformed nitrate and salinity ($NO_3^{pre} \propto -13.1 S_A$, $r^2 = 0.95$, Figure S8f in Supporting Information S1), partially compensated by a weaker positive correlation with regenerated nitrate ($NO_3^{reg} \propto 2.0 S_A$, $r^2 = 0.140$, Figure S8g in Supporting Information S1). The magnitude of nitrate depletion by along-ACC advection, estimated by multiplying the nitrate:salinity slope (-11.1 μmol kg^{-1} (g kg^{-1})$^{-1}$) by the geostrophic salt flux (17 g kg^{-1} m yr^{-1}), is ≈ -0.19 mol m^{-2} yr^{-1}. The magnitude of biological carbon export production in the SAZ is estimated at about 2 molC m^{-2} yr^{-1} (Arteaga et al., 2019; Johnson, Plant, Dunne, et al., 2017), which is equivalent (using a C:N ratio of 106:16) to a nitrate drawdown of $\sim$0.30 mol m^{-2} yr^{-1} from the photic zone. Since a fraction of this nitrate is remineralized above the winter mixed-layer depth, this estimate represents an upper-limit for nitrate drawdown from the upper ocean by biological export, indicating that advection of subtropical waters can be as significant as biological processes for the SAMW nutrient budget. This conclusion is supported by a circumpolar nitrate budget in the SAZ using climatological nutrient data (Garcia et al., 2018) (Figure S11 in Supporting Information S1), which shows that Ekman transport supplies 0.43 mol m^{-2} yr^{-1} of nitrate to the SAZ, opposed at similar rates (≈ -0.15 mol m^{-2} yr^{-1}) by the geotropic flow, eddy transport and a residual term attributed to biological uptake.
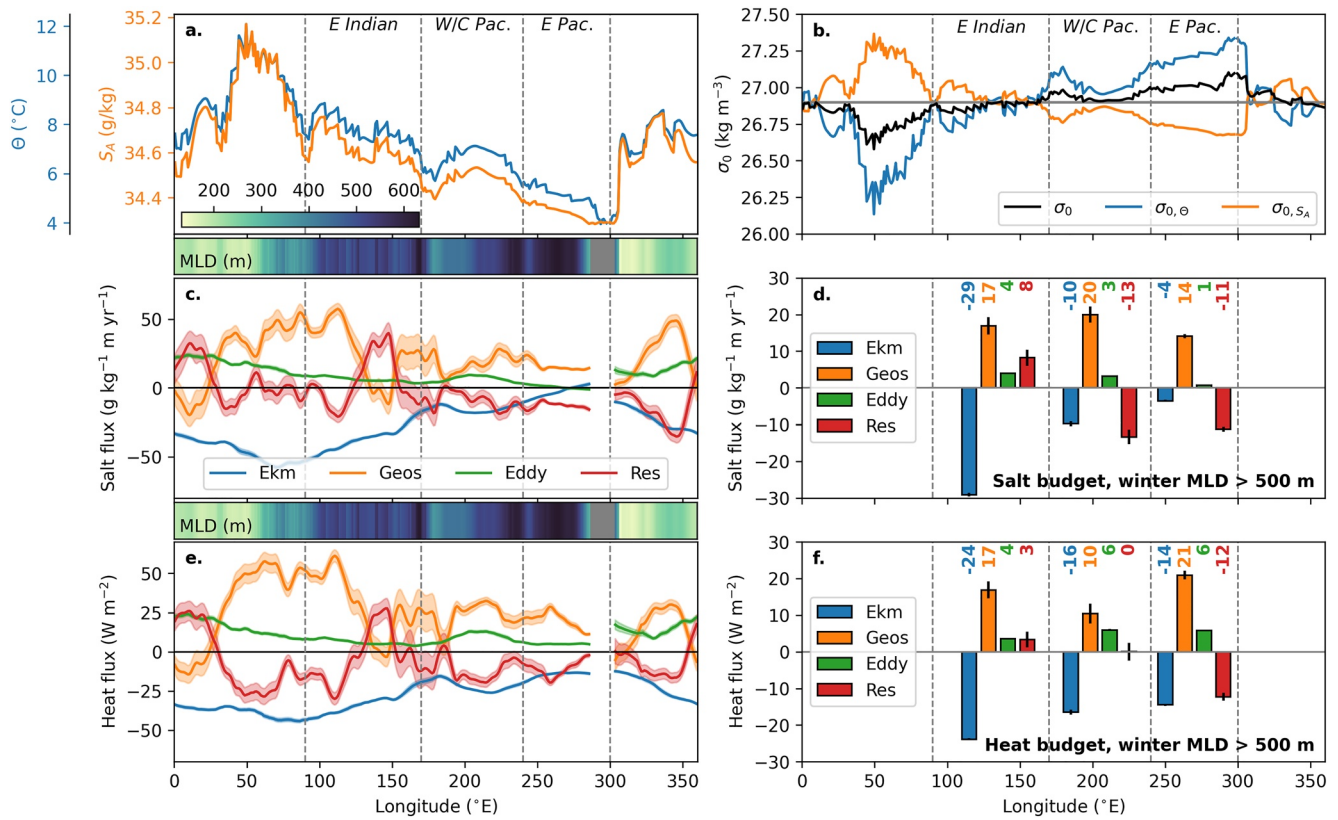
Figure 4. Mean (a) θ, S_A and (b) potential density (σ_0, with contributions from θ and S_A) in the upper 1,000 m of the SAZ (a 5° latitudinal band to north of the SAF, Figure 1a). The annual maximum MLD is shown in color insets. Salinity and heat budget terms averaged in the SAZ (c and e) and in the SAMW formation regions (maximum annual MLD >500 m) (d and f). Error bars represent standard errors. Budget Terms: geostrophic (Geos.), Ekman (Ekm.) and eddy advection, and residual (Res.). Budget terms in c and e were smoothed with a 30-degree running mean.

7. Discussion and Conclusions

Cooling by air-sea fluxes and Ekman transport are often invoked as the main forcing mechanisms driving deep winter mixing in the SAZ, and controlling the spatio-temporal variability of SAMW properties (Gao et al., 2018; Holte et al., 2012; Hong et al., 2020; McCartney, 1977; Naveira Garabato et al., 2009). Implicit in this view is a densification of SAZ waters by these fluxes, which drive the deep convection leading to SAMW production. However, the origin and renewal of SAZ waters has received less attention, except for a few modeling studies illustrating the contribution of along-ACC advection from subtropical-gyre western boundaries, specifically the Agulhas current (Small et al., 2021; Wang et al., 2014). Our analysis supports the generality of this finding, by attributing the subsurface salinity maximum characterizing SAZ deep-convection regions (DuVivier et al., 2018) to advection of warm, saline waters of subtropical origin.

The convergences of heat and salt associated with the northern ACC are linked to the progressive decrease of temperature and salinity along the SAZ (driving a partially compensated density increase), from the western Indian to the eastern Pacific (Figures 4a and 4b). We explain this decrease in temperature and salinity, which shapes the properties of the different SAMW pools (Herraiz-Borreguero & Rintoul, 2011; McCartney, 1977), by the following sequence of processes. First, the northern ACC gains heat and salt through interaction with the western boundary currents –mainly the Agulhas Return current (Pollard & Read, 2001) and, to a lesser extent, the Brazil and East Australian currents (Figure 4a)–, where eddy fluxes are maximal (Figures 4c and 4e). Second, air-sea fluxes and northward Ekman transport drive a progressive freshening and cooling of surface waters along the ACC path. Deep convection across the SAMW density range regularly transfers the gradient created by surface fluxes downward over the seasonal pycnocline. This horizontal gradient supports transport convergence in the seasonal pycnocline, triggering the subsurface salinity maximum formation.

The influx of subtropical waters carries implications for SAMW physical and biogeochemical properties, and for the mixed-layer dynamics controlling SAMW ventilation. The advection of warmer, saltier waters represents a leading-order term in the heat and salt budgets of the SAZ balancing, along with eddy transport, freshening and cooling by Ekman and air-sea fluxes. Although in absolute terms the subtropical content of SAMW decreases eastward from the Indian to the eastern Pacific Ocean (as reflected by decreasing temperature and salinity, Figure 4a), the magnitude of the geostrophic heat and salt convergences is comparable across SAMW formation regions in both basins (Figures 4c–4f), resulting in a similar amplitude of the salinity cycle in the pycnocline (Figures 1, S1 and S2 in Supporting Information S1). The subsurface salinity maximum caps the SAMW pool after winter mixing, enhancing stratification at the mixed-layer base, which hinders mixed-layer deepening in the following fall and winter seasons (Figure 1f). Therefore, the salinity maximum behaves as a gate-keeper of the SAMW pool, potentially acting to inhibit SAMW ventilation in years of weak atmospheric forcing.

From a biogeochemical viewpoint, the influx of subtropical waters reduces nutrient concentrations in SAMW formation regions. SAMW is a major source of nutrients for the global ocean pycnocline, sustaining biological productivity in low-latitude regions (Fripiat et al., 2021; Hauck et al., 2018; Palter et al., 2010; Sarmiento et al., 2004; Williams et al., 2006). The relatively high nutrient concentrations of SAMW are the result of the northward Ekman transport of Antarctic surface waters. As these waters acquire high nutrient levels from upwelling of Circumpolar Deep Water around and south of the ACC, it is widely viewed that SAMW nutrient content is determined by biological consumption during the upwelled waters' northward transit. The degree of biological drawdown depends on several factors, including limiting micronutrients like iron, and the transit time of upwelled waters before subduction, which is related to the strength of meridional overturning. In this framework, decadal- and centennial-scale variations in SAMW nutrient content and low-latitude productivity have been interpreted in terms of such factors (Ayers & Strutton, 2013; Marinov et al., 2006; Nissen et al., 2021; Sarmiento et al., 2004). Our analysis calls for a re-examination of this view by showing that the influx of subtropical waters can be as relevant as biological drawdown in lowering SAMW nutrient concentrations with respect to incoming Antarctic waters. The redistribution of nutrients between high and low latitudes may thus be subjected to additional climate sensitivities and feedback mechanisms involving the gyre circulation, not considered in the current overturning-centered paradigm.

The along-ACC advection of warm, salty and nutrient poor waters of subtropical origin described here provides a dynamic link between the western boundary currents and the SAMW formation regions, consistent with the delayed connections (with a lag of a few years) between them identified with an adjoint ocean model (Boland et al., 2021). Our findings suggest that this long-range connection is of primary relevance for SAMW dynamics and their physical and biogeochemical characteristics, potentially influencing the drawdown of heat, carbon and nutrients into the global pycnocline. The eastward transport along the ACC's northern flank may have accelerated in recent decades as a result of ocean warming (Shi et al., 2021), which could have enhanced the subtropical contribution to SAMW. These changes should be considered alongside local wind and buoyancy forcing, when assessing the influence of natural climate variability and anthropogenic climate change on SAMW formation rates and properties. The mechanistic understanding gained here through the analysis of biogeochemical float data should contribute to the assessment and advancement of the representation of SAMW in ocean models (Hong et al., 2021; Sallée et al., 2013), which is key to understanding and predicting the impacts of these changes.

Data Availability Statement

The SOCCOM data set used in this study was published on May 2021 with doi: 10.6075/J0T43SZG and is available at https://soccompu.princeton.edu/www/index.html. Data from the iteration 133 of B-SOSE can downloaded from http://sose.ucsd.edu/BSOSE6_iter133_solution.html. The Roemmich and Gilson (2009) climatological data can be obtained from http://sio-argo.ucsd.edu/RG_Climatology.html. Additional Argo data were collected and made freely available by the International Argo Program and the national programs that contribute to it (http://www.argo.ucsd.edu, http://argo.jcommops.org). The Argo Program is part of the Global Ocean Observing System.

References

Arteaga, L. A., Pahlow, M., Bushinsky, S. M., & Sarmiento, J. L. (2019). Nutrient controls on export production in the Southern Ocean. *Global Biogeochemical Cycles*, *33*(8), 942–956. https://doi.org/10.1029/2019GB006236

Ayers, J. M., & Strutton, P. G. (2013). Nutrient variability in subantarctic mode waters forced by the southern annular mode and ENSO. *Geophysical Research Letters*, *40*(13), 3419–3423. https://doi.org/10.1002/grl.50638

Boland, E. J. D., Jones, D. C., Meijers, A. J. S., Forget, G., & Josey, S. A. (2021). Local and remote influences on the heat content of Southern Ocean mode water formation regions. *Journal of Geophysical Research: Ocean*, *126*(4), 1–25. https://doi.org/10.1029/2020JC016585

de BoyerMontégut, C. (2004). Mixed layer depth over the global ocean: An examination of profile data and a profile-based climatology. *Journal of Geophysical Research*, *109*(C12), C12003. https://doi.org/10.1029/2004JC002378

DuVivier, A. K., Large, W. G., & Small, R. J. (2018). Argo observations of the deep mixing band in the Southern Ocean: A salinity modeling challenge. *Journal of Geophysical Research: Ocean*, *123*(10), 7599–7617. https://doi.org/10.1029/2018JC014275

Fripiat, F., Martínez-García, A., Marconi, D., Fawcett, S. E., Kopf, S. H., Luu, V. H., et al. (2021). Nitrogen isotopic constraints on nutrient transport to the upper ocean. *Nature Geoscience*, *14*(11), 855–861. https://doi.org/10.1038/s41561-021-00836-8

Gao, L., Rintoul, S. R., & Yu, W. (2018). Recent wind-driven change in Subantarctic Mode Water and its impact on ocean heat storage. *Nature Climate Change*, *8*, 58–63. https://doi.org/10.1038/s41558-017-0022-8

Garcia, H., Weathers, K., Paver, C., Smolyar, I., Boyer, T., Locarnini, R., & Reagan, J. (2018). World ocean atlas 2018. Volume 4: Dissolved inorganic nutrients (phosphate, nitrate and nitrate+nitrite, silicate). *NOAA Atlas NESDIS*, *84*, 35.

Gent, P. R., & McWilliams, J. C. (1990). Isopycnal mixing in ocean circulation models. *Journal of Physical Oceanography*, *20*(1), 150–155. https://doi.org/10.1175/1520-0485(1990)020<0150:IMIOCM>2.0.CO;2

Gille, S. T., Sheen, K. L., Swart, S., & Thompson, A. F. (2022). Mixing in the Southern Ocean. In *Ocean mix*ing: rivers, mechanisms and impacts (pp. 301–327). Elsevier Inc. https://doi.org/10.1016/b978-0-12-821512-8.00019-0

Groeskamp, S., Lenton, A., Matear, R., Sloyan, B. M., & Langlais, C. (2016). Anthropogenic carbon in the ocean—surface to interior connections. *Global Biogeochemical Cycles*, *30*(11), 1682–1698. https://doi.org/10.1002/2016GB005476

Gruber, N., Clement, D., Carter, B. R., Feely, R. A., van Heuven, S., Hoppema, M., et al. (2019). The oceanic sink for anthropogenic CO_2 from 1994 to 2007. *Science*, *363*(6432), 1193–1199. https://doi.org/10.1126/science.aau5153

Hanawa, K., & Talley, L. D. (2001). Chapter 5.4 mode waters. *International Geophysics*, *77*, 373–386. https://doi.org/10.1016/S0074-6142(01)80129-7

Hauck, J., Lenton, A., Langlais, C., & Matear, R. (2018). The fate of carbon and nutrients exported out of the Southern Ocean. *Global Biogeochemical Cycles*, *32*(10), 1556–1573. https://doi.org/10.1029/2018GB005977

Hauck, J., Völker, C., Wang, T., Hoppema, M., Losch, M., & Wolf-Gladrow, D. A. (2013). Seasonally different carbon flux changes in the Southern Ocean in response to the southern annular mode. *Global Biogeochemical Cycles*, *27*(4), 1236–1245. https://doi.org/10.1002/2013GB004600

Herraiz-Borreguero, L., & Rintoul, S. R. (2010). Subantarctic mode water variability influenced by mesoscale eddies south of Tasmania. *Journal of Geophysical Research: Ocean*, *115*(C4), C04004. https://doi.org/10.1029/2008JC005146

Herraiz-Borreguero, L., & Rintoul, S. R. (2011). Subantarctic mode water: Distribution and circulation. *Ocean Dynamics*, *61*, 103–126. https://doi.org/10.1007/s10236-010-0352-9

Holte, J. W., & Talley, L. (2009). A new algorithm for finding mixed layer depths with applications to argo data and subantarctic mode water formation. *Journal of Atmospheric and Oceanic Technology*, *26*(9), 1920–1939. https://doi.org/10.1175/2009JTECHO543.1

Holte, J. W., Talley, L. D., Chereskin, T. K., & Sloyan, B. M. (2012). The role of air-sea fluxes in Subantarctic Mode Water formation. *Journal of Geophysical Research: Ocean*, *117*(C3), C03040. https://doi.org/10.1029/2011JC007798

Holte, J. W., Talley, L. D., Chereskin, T. K., & Sloyan, B. M. (2013). Subantarctic mode water in the southeast Pacific: Effect of exchange across the subantarctic front. *Journal of Geophysical Research: Ocean*, *118*(4), 2052–2066. https://doi.org/10.1002/jgrc.20144

Hong, Y., Du, Y., Qu, T., Zhang, Y., & Cai, W. (2020). Variability of the subantarctic mode water volume in the south Indian ocean during 2004–2018. *Geophysical Research Letters*, *47*(10). https://doi.org/10.1029/2020GL087830

Hong, Y., Du, Y., Xia, X., Xu, L., Zhang, Y., & Xie, S.-P. (2021). Subantarctic mode water and its long-term change in CMIP6 models. *Journal of Climate*, *34*(23), 9385–9400. https://doi.org/10.1175/JCLI-D-21-0133.1

Iudicone, D., Rodgers, K. B., Plancherel, Y., Aumont, O., Ito, T., Key, R. M., et al. (2016). The formation of the ocean's anthropogenic carbon reservoir. *Scientific Reports*, *6*, 35473. https://doi.org/10.1038/srep35473

Iudicone, D., Rodgers, K. B., Stendardo, I., Aumont, O., Madec, G., Bopp, L., et al. (2011). Water masses as a unifying framework for understanding the Southern Ocean carbon cycle. *Biogeosciences*, *8*(5), 1031–1052. https://doi.org/10.5194/bg-8-1031-2011

Jackett, D. R., & McDougall, T. J. (1997). A neutral density variable for the world's oceans. *Journal of Physical Oceanography*, *27*(2), 237–263. https://doi.org/10.1175/1520-0485(1997)027<0237:ANDVFT>2.0.CO;2

Johnson, K. S., Plant, J. N., Coletti, L. J., Jannasch, H. W., Sakamoto, C. M., Riser, S. C., et al. (2017). Biogeochemical sensor performance in the SOCCOM profiling float array. *Journal of Geophysical Research: Ocean*, *122*(8), 6416–6436. https://doi.org/10.1002/2017JC012838

Johnson, K. S., Plant, J. N., Dunne, J. P., Talley, L. D., & Sarmiento, J. L. (2017). Annual nitrate drawdown observed by SOCCOM profiling floats and the relationship to annual net community production. *Journal of Geophysical Research: Ocean*, *122*(8), 6668–6683. https://doi.org/10.1002/2017JC012839

Jones, D. C., Meijers, A. J. S., Shuckburgh, E., Sallée, J.-B., Haynes, P., McAufield, E. K., & Mazloff, M. R. (2016). How does subantarctic mode water ventilate the southern hemisphere subtropics? *Journal of Geophysical Research: Ocean*, *121*(9), 6558–6582. https://doi.org/10.1002/2016JC011680

Li, Z., England, M. H., Groeskamp, S., Cerovečki, I., & Luo, Y. (2021). The origin and fate of subantarctic mode water in the Southern Ocean. *Journal of Physical Oceanography*, *51*(9), 2951–2972. https://doi.org/10.1175/JPO-D-20-0174.1

Marinov, I., Gnanadesikan, A., Toggweiler, J. R., & Sarmiento, J. L. (2006). The Southern Ocean biogeochemical divide. *Nature*, *441*, 964–967. https://doi.org/10.1038/nature04883

Marshall, J., & Speer, K. (2012). Closure of the meridional overturning circulation through Southern Ocean upwelling. *Nature Geoscience*, *5*(3), 171–180. https://doi.org/10.1038/ngeo1391

McCartney, M. S. (1977). Antarctic mode water. *Journal of Marine Research*, *76*(3–4).

McCartney, M. S. (1982). The subtropical recirculation of mode waters. *Journal of Marine Research*, *40*(436), 427–464.

McDougall, T. J., & Barker, P. M. (2011). *Getting started with TEOS-10 and the Gibbs Seawater (GSW) Oceanographic Toolbox* (p. 28). Scor/Iapso Wg127(July).

Meijers, A. J., Cerovečki, I., King, B. A., & Tamsitt, V. (2019). A see-saw in Pacific subantarctic mode water formation driven by atmospheric modes. *Geophysical Research Letters*, *46*(22), 13152–13160. https://doi.org/10.1029/2019GL085280

Morrison, A. K., Waugh, D. W., Hogg, A. M., Jones, D. C., & Abernathey, R. P. (2022). Ventilation of the Southern Ocean pycnocline. *Annual Review of Marine Science*, *14*, 405–430. https://doi.org/10.1146/annurev-marine-010419-011012

Naveira Garabato, A. C., Jullion, L., Stevens, D. P., Heywood, K. J., & King, B. A. (2009). Variability of subantarctic mode water and Antarctic intermediate water in the Drake passage during the late-twentieth and early-twenty-first centuries. *Journal of Climate*, *22*(13), 3661–3688. https://doi.org/10.1175/2009JCLI2621.1

Nissen, C., Gruber, N., Münnich, M., & Vogt, M. (2021). Southern Ocean phytoplankton community structure as a gatekeeper for global nutrient biogeochemistry. *Global Biogeochemical Cycles*, *35*(8), 1–23. https://doi.org/10.1029/2021GB006991

Palter, J. B., Sarmiento, J. L., Gnanadesikan, A., Simeon, J., & Slater, R. D. (2010). Fueling export production: Nutrient return pathways from the deep ocean and their dependence on the Meridional Overturning Circulation. *Biogeosciences*, *7*(11), 3549–3568. https://doi.org/10.5194/bg-7-3549-2010

Pollard, R. T., & Read, J. F. (2001). Circulation pathways and transports of the Southern Ocean in the vicinity of the southwest Indian ridge. *Journal of Geophysical Research: Ocean*, *106*(C2), 2881–2898. https://doi.org/10.1029/2000jc900090

Portela, E., Kolodziejczyk, N., Maes, C., & Thierry, V. (2020). Interior water-mass variability in the Southern Hemisphere oceans during the last decade. *Journal of Physical Oceanography*, *50*(2), 361–381. https://doi.org/10.1175/JPO-D-19-0128.1

Qu, T., Gao, S., & Fine, R. A. (2020). Variability of the sub-Antarctic mode water subduction rate during the Argo period. *Geophysical Research Letters*, *47*(13). https://doi.org/10.1029/2020GL088248

Rintoul, S. R., & England, M. H. (2002). Ekman transport dominates local air–sea fluxes in driving variability of subantarctic mode water. *Journal of Physical Oceanography*, *32*(5), 1308–1321. https://doi.org/10.1175/1520-0485(2002)032<1308:ETDLAS>2.0.CO;2

Roemmich, D., Church, J., Gilson, J., Monselesan, D., Sutton, P., & Wijffels, S. (2015). Unabated planetary warming and its ocean structure since 2006. *Nature Climate Change*, *5*(3), 240–245. https://doi.org/10.1038/nclimate2513

Roemmich, D., & Gilson, J. (2009). The 2004-2008 mean and annual cycle of temperature, salinity, and steric height in the global ocean from the Argo Program. *Progress in Oceanography*, *82*(2), 81–100. https://doi.org/10.1016/j.pocean.2009.03.004

Ross, O. N., & Sharples, J. (2004). Recipe for 1-D Lagrangian particle tracking models in space-varying diffusivity. *Limnology and Oceanography: Methods*, *2*(9), 289–302. https://doi.org/10.4319/lom.2004.2.289

Sabine, C. L., Feely, R. A., Gruber, N., Key, R. M., Lee, K., Bullister, J. L., et al. (2004). The oceanic sink for anthropogenic CO2. *Science*, *305*(5682), 367–371. https://doi.org/10.1126/science.1097403

Sallée, J. B., Morrow, R., & Speer, K. (2008). Eddy heat diffusion and subantarctic mode water formation. *Geophysical Research Letters*, *35*(5), L05607. https://doi.org/10.1029/2007GL032827

Sallée, J. B., Shuckburgh, E., Bruneau, N., Meijers, A. J., Bracegirdle, T. J., Wang, Z., & Roy, T. (2013). Assessment of Southern Ocean water mass circulation and characteristics in CMIP5 models: Historical bias and forcing response. *Journal of Geophysical Research: Ocean*, *118*(4), 1830–1844. https://doi.org/10.1002/jgrc.20135

Sallée, J.-B., Speer, K., Rintoul, S., & Wijffels, S. (2010). Southern Ocean thermocline ventilation. *Journal of Physical Oceanography*, *40*(3), 509–529. https://doi.org/10.1175/2009JPO4291.1

Sarmiento, J., Gruber, N., Brzezinski, A., & Dunne, J. (2004). High latitude controls of thermocline nutrients and low latitude biological productivity. *Nature*, *427*(6969), 56–60. https://doi.org/10.1038/nature02127

Shi, J.-r., Talley, L. D., Xie, S.-P., Peng, Q., & Liu, W. (2021). Ocean warming and accelerating Southern Ocean zonal flow. *Nature Climate Change*, *11*(12), 1090–1097. https://doi.org/10.1038/s41558-021-01212-5

Sloyan, B. M., & Rintoul, S. R. (2001). Circulation, renewal, and modification of Antarctic mode and intermediate water. *Journal of Physical Oceanography*, *31*(4), 1005–1030. https://doi.org/10.1175/1520-0485(2001)031<1005:CRAMOA>2.0.CO;2

Small, R. J., DuVivier, A. K., Whitt, D. B., Long, M. C., Grooms, I., & Large, W. G. (2021). On the control of subantarctic stratification by the ocean circulation. *Climate Dynamics*, *56*, 299–327. https://doi.org/10.1007/s00382-020-05473-2

Talley, L. D., Rosso, I., Kamenkovich, I., Mazloff, M. R., Wang, J., Boss, E., et al. (2019). Southern Ocean biogeochemical float deployment strategy, with example from the Greenwich meridian line (GO-SHIP A12). *Journal of Geophysical Research: Ocean*, *124*(1), 403–431. https://doi.org/10.1029/2018JC014059

Tamsitt, V., Talley, L. D., Mazloff, M. R., & Cerovecki, I. (2016). Zonal variations in the Southern Ocean heat budget. *Journal of Climate*, *29*(18), 6563–6579. https://doi.org/10.1175/JCLI-D-15-0630.1

Verdy, A., & Mazloff, M. R. (2017). A data assimilating model for estimating Southern Ocean biogeochemistry. *Journal of Geophysical Research: Ocean*, *122*(9), 6968–6988. https://doi.org/10.1002/2016JC012650

Visbeck, M., Marshall, J., Haine, T., & Spall, M. (1997). Specification of eddy transfer coefficients in coarse-resolution ocean circulation models. *Journal of Physical Oceanography*, *27*(3), 381–402. https://doi.org/10.1175/1520-0485(1997)027<0381:SOETCI>2.0.CO;2

Wang, J., Mazloff, M. R., & Gille, S. T. (2014). Pathways of the Agulhas waters poleward of 29°S. *Journal of Geophysical Research: Ocean*, *119*(7), 4234–4250. https://doi.org/10.1002/2014JC010049

Williams, R. G., & Follows, M. J. (2011). *Ocean dynamics and the carbon cycle: Principles and mechanisms*. Cambridge University Press. https://doi.org/10.1017/CBO9780511977817

Williams, R. G., Roussenov, V., & Follows, M. J. (2006). Nutrient streams and their induction into the mixed layer. *Global Biogeochemical Cycles*, *20*(1), 1–18. https://doi.org/10.1029/2005GB002586

Williams, R. G., Spall, M. A., & Marshall, J. C. (1995). Does Stommel's mixed layer "demon" work? *Journal of Physical Oceanography*, *25*(12), 3089–3102. https://doi.org/10.1175/1520-0485(1995)025<3089:DSMLW>2.0.CO;2

Reference From the Supporting Information

Chelton, D. B., DeSzoeke, R. A., Schlax, M. G., ElNaggar, K., & Siwertz, N. (1998). Geographical variability of the first baroclinic Rossby radius of deformation. *Journal of Physical Oceanography*, *28*(3), 433–460. https://doi.org/10.1175/1520-0485(1998)0280433